

# A Physics-Based Dual Deformable Model

Stelios Krinidis and Vassilios Chatzis

Information Management Department  
Technological Institute of Kavala  
Ag. Loukas, 65404, Kavala, Greece  
stelios.krinidis@mycosmos.gr; chatzis@teikav.edu.gr

Received December 2010; revised November 2011

---

**ABSTRACT.** *This paper presents a novel physics-based dual deformable model to detect objects in an image. This model is more efficient than the known methods since it can detect objects whose boundaries are not necessarily defined by gradient. It minimizes an energy which can be seen as a particular case of a minimal partition problem. This energy is used as the model motivation power evolving the deformable model, which will stop on the desired object boundary. However, the stopping term does not depend on the gradient of the image, as most of the classical active and deformable contour models, but instead is related to the image color and spatial segments. Modal analysis is exploited to solve the deformation equation. Furthermore, the segmentation result produced depends on the physical characteristics of the model. Different physical characteristics lead to different segmentation results. The introduced deformable dual model composes of three interconnected deformable models. In most cases, one model expands from inside to the desired image features, the other contracts from outside, and finally, the deformation of the intermediate model is controlled by the two others, via modal analysis, to the desired image features. The whole model interconnection idea provides a balanced technique with a strong ability to reject “weak” local minima improving the performance of the segmentation against other known methods. The theoretical properties and various experiments presented demonstrate that the proposed dual deformable model is better and more robust than other known methods.*

**Keywords:** Deformable model, dual active contours, modal analysis, deformable curves, segmentation.

---

1. **Introduction.** Image segmentation is one of the first and most important tasks in image analysis and computer vision. In the computer vision literature, various methods have been proposed for object segmentation and feature extraction [1]. However, the design of robust and efficient segmentation algorithms is still a very challenging research topic, due to the variety and complexity of images.

Since the introduction of snakes [2], active contours have been applied to a variety of problems in image processing and computer vision such as segmentation and feature extraction, image registration, shape analysis and modeling, and visual tracking.

The basic idea in active contour models or snakes is to evolve a curve, in order to detect objects in the image under consideration. For instance, starting with a curve around the object to be detected, the curve moves toward its interior normal and has to stop on the boundary of the object. The original snake model was formulated to minimize the energy functional:

$$E(C) = a \int_0^1 |C'(s)|^2 ds + \beta \int_0^1 |C''(s)|^2 ds + \lambda \int_0^1 P(C(s)) ds, \quad (1)$$

where  $a, \beta$  and  $\lambda$  are real positive weighting constants,  $C : [0, 1] \rightarrow \mathbb{R}^2$  is a parameterized curve, and  $P(C)$  is a potential which depends upon some desirable image features. In (1), the first two terms are internal forces, which control the regularity of the active contour (curve  $C$ ), while the potential  $P$  attracts the curve  $C$  toward the desired boundary. Normally, the potential  $P$  is an edge-function, based on the gradient of the processed image.

It is common knowledge, that the original snake models had difficulty dealing with topology changes, since they were dependent upon an arbitrary parameterization of the curve. Geometric active contour models, such as [3, 4], were introduced shortly afterwards based on curve evolution theory, which could also handle topology changes very naturally when implemented using level set methods proposed by Osher and Sethian [5].

The geometric active contour model most closely related to the original snake model is probably the *geodesic active contour* model [6, 7, 8], which has been based on the curvature of the image and to an *inflationary force* [9].

Both the original snakes as well as geodesic active contours are prone to getting “trapped” by extraneous edges due to image noise or texture, yielding many undesirable local minima of their corresponding energy functionals. As a consequence, initializations of the models must be very carefully chosen. Depending on the initial placement of the variational active contour models, whose data-dependent energy functionals are designed to converge to local minima, active contours could be driven to the “desired” global minimum or to any other local minimum due to the noise or complex image structure. Thus, the already existed active contour algorithms would be enriched with energy functionals free of any kind of sensitivity to local minima.

Cohen et al. [10, 11] has proposed the minimal path technique, which captures the global minimum of a contour energy between two fixed user-defined end points. In this technique, the image is defined as an oriented graph characterized by its cost function, and the object boundary detection becomes the optimal path search problem between two user-defined points in the graph. This approach leads the snake-like energy to a global minimum, avoiding any local minima. However, this technique is semi-automatic, since it requires the user interference to locate the end-points precisely on the desired object boundary. Also, the extension of the method to closed curve extraction needs a topology-based saddle search routine.

Other implementations have also been proposed for capturing more global minimizers by restricting the search space. Dual snakes, proposed by Gunn and Nixon [12, 13], is such a method. This method uses two interlinked snakes instead of one. The first is set inside the desired object and expands, and the second is set outside and moves inward. The two snakes are interlinked by arc-length and reach the inner and outer boundaries of the desired object, respectively. Similar methods were also proposed in [14, 15, 16, 17], which restrict their search spaces exploiting normals lengths on the initial contour. Another approach restricting the search space is the dual-band active contour [18], which exploits predefined width chosen by the Euclidean distance transform of the initial contour as a means to restrict the search space. Although these methods may find more desirable minima for some images, they have several drawbacks. One is the choice of the search space, i.e., the desired boundary should be included in the search space. Another is that these methods are restricted to detection of objects with simple topologies.

All these classical snakes and active contour models are known as “edge-based” models, since they rely on edge-functionals, depending on the image gradient, to stop the curve evolution. Also, these models can detect only objects with edges defined by gradient. In practice, the discrete gradients are bounded and then the stopping function is never zero on the edges, and the curve may pass through the boundary [3, 4]. If the image under consideration is very noisy, then the isotropic smoothing Gaussian has to be strong, which will smooth the edges too. Thus, the performance of the purely edge-based models is often inadequate. Thus, there has been much research into the design of complex region-based energy functionals that are less likely to yield undesirable local minima when compared to simpler edge-based energy functionals. In general, region-based models [20]-[27] utilize image information not only near the evolving contour, but image statistics inside and outside the contour as well in order to achieve better performance. Many of these methods were inspired by the “Region Competition” algorithm presented by Zhu and Yuille [28]. Unfortunately, most of these more “robust” region-based energy functionals assume highly constrained models for pixel intensities within each region.

This paper deals with the above mentioned problems. It presents a novel physics-based dual deformable model for image segmentation with better performance than the existing methods, since it can handle objects whose boundaries are not necessarily defined by gradient. The objects of the image are extracted by the equilibrium state of the deformations of a 2D finite element based model. The dual deformable model evolves and reaches, finally, the equilibrium state minimizing an energy which can be seen as a particular case of a minimal partition problem. Deformation equations are solved exploiting modal analysis. The introduced dual deformable model comprises of three interlinked deformable models. In most cases, one model expands from inside to the desired image features, the other contracts from outside, and finally, the intermediate model is deformed by the others, via modal analysis, to the desired image features. Experiments show that the whole model interconnection idea provides a balanced technique with a strong ability to reject “weak” local minima. Furthermore, the physical characteristics of the deformable model determine how detailed the segmentation would be, as well as, how resistant the model would be to noise. Also, different image segmentations can be achieved by the same method only varying the physical characteristics of the dual deformable model used.

The proposed approach was motivated by the technique presented in [29], which determines correspondences between objects features using eigen-decomposition analysis. However, the proposed method determines the objects of an image, exploiting the frequency-based features, obtained by the free vibrations of a physics-based modeling [30, 31, 32] adapted on the contour of the objects under consideration. Modal features using physics-based models assist our method to be robust to noise and shape variations.

The remainder of the paper is organized as follows. The 2D physics-based dual deformable model [31] is presented in Section 2. In Section 3, the motivation energy minimization problem is introduced. Experimental results are presented in Section 4 and conclusions are drawn in Section 5.

**2. 2D Physics-Based Dual Deformable Model.** In this Section, the physics-based dual deformable model exploiting modal analysis, whose deformations are used in order to extract the object, will be briefly reviewed. More details regarding the deformation process and all the adopted assumptions are presented in [31, 32].

Modelling an elastic 2D boundary can be achieved by a single closed chain topology of  $N$  virtual masses on the contour. In our dual deformable model, the term “dual” is not used as a mathematical concept, but to describe the two models: an interior model (inner) lies within the region of the desired feature and an exterior (outer) outside it (Figure 1).

A third one (intermediate model) lies between them. Each model node has a mass  $m$  and is connected to its two neighbors with identical springs of stiffness  $k$ . Furthermore, the three models are coupled using springs with the same characteristics, which cause the models to be attracted to each other as well as to suitable image features. The ratio  $a = \frac{k}{m}$  constitutes the so-called characteristic value of the model, which is a constant value that describes its physical characteristics and determines its physical behavior. When  $a$  increases, the object tends to behave as a rigid one, which means in practice, that the model can be spatially moved without any deformation. On the other hand, when  $a$  decreases, model tends to be treated as a fully deformable one, which means that each force affects only the node (mass) it is applied to. Furthermore, these model nodes are points on the object contour at equilibrium and do not represent interior object regions. The node coordinates of the model under examination are stacked in vector:

$$V_t = [v_{11}^t, v_{12}^t, \dots, v_{1N}^t, v_{21}^t, \dots, v_{2N}^t, v_{31}^t, \dots, v_{3N}^t]^T, \quad (2)$$

where  $N$  is the number of vertices (masses) of each single model (the dual model has  $3N$  nodes),  $t$  denotes the  $t$ -th deformation time instance, and  $v_{0,i}^t = [x_{1,i}^t, y_{1,i}^t]^T$ . The  $v_{0,i}^t$

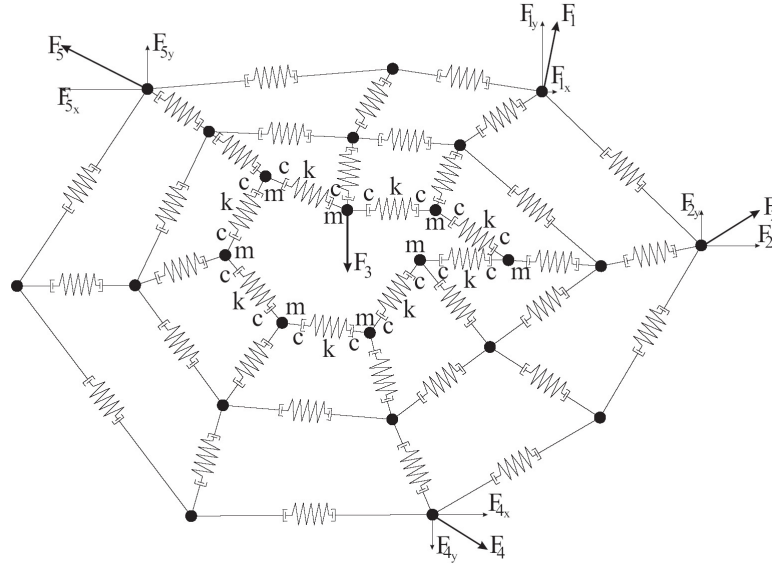


FIGURE 1. 2D dual model example of 8 nodes per single model (outer, inner and intermediate) of mass  $m$  connected with identical springs of stiffness  $k$ . Five forces are acting on the model, that produce model deformation.

represents the  $i$ -th node of the outer model, the  $v_{m,i}^t$  the  $i$ -th node of the intermediate model and  $v_{i,i}^t$  the  $i$ -th node of the inner model. The model under study, is a physics-based system governed by the fundamental equation of dynamics, which can be written in a matrix form [33]:

$$\mathbf{M}\ddot{\mathbf{u}} + \mathbf{C}\dot{\mathbf{u}} + \mathbf{K}\mathbf{u} = \mathbf{f}_t, \quad (3)$$

where  $\mathbf{u} = \mathbf{v}_t - \mathbf{v}_{t_0}$  is the nodal displacements vector.  $\mathbf{M}$ ,  $\mathbf{C}$ , and  $\mathbf{K}$  [31, 32, 33, 34] are the mass, damping, and stiffness matrices of the model, respectively, and  $\mathbf{f}_t$  is the external force vector, usually resulting from the attraction of the model by the object contour (sometimes based on the Euclidean distance between the object contour and the node coordinates [35, 36]). Equation (3) is a finite element formulation of the deformation process.

Instead of solving directly the equilibrium equation (3), one can transform it by a change of basis:

$$\mathbf{u} = \Psi \tilde{\mathbf{u}}, \quad (4)$$

where  $\Psi$  is the square nonsingular transformation matrix of order  $3N$  to be determined, and  $\tilde{\mathbf{u}}$  is referred to as the generalized displacement vector. One effective way of choosing  $\Psi$  is setting it equal to  $\Gamma$ , a matrix whose entries are the eigenvectors of the generalized eigenproblem:

$$\mathbf{K}\gamma_i = \omega_i^2 \mathbf{M}\gamma_i. \quad (5)$$

Thus, equation (4) is transformed to:

$$\mathbf{u} = \Gamma \tilde{\mathbf{u}} = \sum_{i=1}^{3N} \tilde{u}_i \gamma_i. \quad (6)$$

Equation (6) is referred to as the modal superposition equation. The  $i$ -th eigenvector, i.e. the  $i$ -th column of  $\Gamma$ , denoted by  $\gamma_i$ , is also called the  $i$ -th vibration mode, is also called the  $i$ -th *vibration mode*,  $\tilde{u}_i$  (the  $i$ -th scalar component of  $\tilde{\mathbf{u}}$ ) is its amplitude, and  $\omega_i$  is the corresponding eigenvalue (also called *frequency*). Using the standard Rayleigh hypothesis [31], matrices  $\mathbf{K}$ ,  $\mathbf{M}$  and  $\mathbf{C}$  are simultaneously diagonalized:

$$\begin{cases} \Gamma^T \mathbf{M} \Gamma = \mathbf{I} \\ \Gamma^T \mathbf{K} \Gamma = \Omega^2 \end{cases}, \quad (7)$$

where  $\Omega^2$  is a diagonal matrix whose elements are the eigenvalues  $\omega_i^2$  and  $\mathbf{I}$  is the identity matrix. Thus, in the modal space the governing matrix-form, equations decoupled into  $3N$  scalar equations, by substituting (6) into (3) and premultiplying by  $\Gamma^T$ :

$$\ddot{\tilde{\mathbf{u}}} + \tilde{\mathbf{C}} \dot{\tilde{\mathbf{u}}} + \Omega^2 \tilde{\mathbf{u}} = \tilde{\mathbf{f}}, \quad (8)$$

where  $\tilde{\mathbf{C}} = \Gamma^T \mathbf{C} \Gamma$  and  $\tilde{\mathbf{f}} = \Gamma^T \mathbf{f}$ . Solving these equations at time  $t$  leads to  $\tilde{\mathbf{u}}$  and the displacement  $\mathbf{u}$  of the model nodes is obtained by the modal superposition equation (6).

In practice, we wish to approximate nodal displacements  $\mathbf{u}$  by  $\tilde{\mathbf{u}}$ , which is the truncated sum of the  $3N$  low-frequency vibration modes, where  $3N' \ll 3N$  :

$$\mathbf{u} \approx \hat{\mathbf{u}} = \sum_{i=1}^{3N'} \tilde{u}_i \gamma_i \quad (9)$$

Eigenvectors  $(\gamma_i)_{i=1, \dots, 3N'}$  form the reduced modal basis of the system. This is the major advantage of modal analysis: it is solved in a subspace corresponding to the  $3N$  truncated low-frequency vibration modes of the deformable structure [31, 32, 37]. The number of vibration modes retained in the object description, is chosen so as to obtain a compact but adequately accurate representation. A typical a priori value for  $N$ , covering many types of standard deformations is equal to one quarter of the number of the vibration modes ( $N$ ).

An important advantage of the formulations described so far, in the full as well as the truncated modal space, is that the vibration modes  $\phi_i$  and the frequencies  $\omega_i$  of a chain topology have an explicit expression [31] and they do not have to be computed using eigen-decomposition techniques (due to the dimensions of matrices  $\mathbf{K}$  and  $\mathbf{M}$ ). The eigenvalues (frequencies) are given by:

$$\omega_{i',i}^2 = 4a \left[ \sin^2 \left( \frac{\pi i'}{6} \right) + \sin^2 \left( \frac{\pi i}{N} \right) \right], \quad (10)$$

and the eigenvectors (vibration modes) are obtained by:

$$\lambda_{i',i} = \left[ \dots, \cos \frac{\pi (2i' - 1) j'}{6} \cos \frac{2\pi i j}{N}, \dots \right]^T, \quad (11)$$

where  $i \in \{1, 2, \dots, N\}$ ,  $i' \in \{1, 2, 3\}$ , and  $j \in \mathcal{B}(N)$ ,  $j' \in \{0, 1, 2\}$ .  $\mathcal{B}(N)$  is the first Brillouin zone [31] and is equal to  $\{-\frac{N}{2} + 1, \dots, \frac{N}{2}\}$  for  $N$  even, and  $\{-\frac{N-1}{2}, \dots, \frac{N-1}{2}\}$  for  $N$  odd. This is one of the main reasons we have chosen and used the dual model topology to parameterize our objects under examination.

In many computer vision applications [32], when the initial and the final deformable contour states are known, it is assumed that a constant force load  $\mathbf{f}$  is applied to the contour model. Thus, equation (3) is called the equilibrium governing equation and corresponds to the static problem:

$$\mathbf{K}\mathbf{u} = \mathbf{f}. \quad (12)$$

In the new basis, equation (12) is simplified to  $2P3N$  scalar equations:

$$\omega_i^2 \tilde{u}_i = \tilde{f}_i. \quad (13)$$

In equation (13),  $\omega_i$  designates the  $i$ -th eigenvalue and the scalar  $\tilde{u}_i$  is the amplitude of the corresponding vibration mode (corresponding to eigenvector  $\gamma_i$ ). Equation (13), indicates that, instead of computing the displacements vector  $\mathbf{u}$  from equation (12), we can compute its decomposition in terms of the vibration modes of the original circular model. Thus, the physical representation  $\mathbf{v}(\tilde{\mathbf{u}})$  is finally given by applying the deformations to the initial position of the dual model:

$$\mathbf{v}(\tilde{\mathbf{u}}) = \mathbf{v}_0 + \mathbf{\Gamma}\tilde{\mathbf{u}}. \quad (14)$$

### 3. Description of the Dual Deformable Model Motivation Energy.

**3.1. The Main Idea.** The dual deformation model exploits the following simple observation. Given an image  $I$ , let us define the evolving two closed curves  $C_{out}$  and  $C_{in}$  (outer and inner deformable models) in  $I$ .

The proposed approach is based on the minimization of a model energy. Let us define the functionals  $F_i$  to be:

$$F_1(C_{out}, C_{in}) = \int_{\substack{outside(C_{out}) \\ outside(C_{in})}} |I(x, y) - c_1|^2 dx dy$$

$$F_2(C_{out}, C_{in}) = \int_{\substack{inside(C_{out}) \\ outside(C_{in})}} |I(x, y) - c_2|^2 dx dy$$

$$F_3(C_{out}, C_{in}) = \int_{\substack{inside(C_{out}) \\ inside(C_{in})}} |I(x, y) - c_3|^2 dx dy$$

where  $c_i$  are constants expressing the average value of the image regions defined by the models. That is,  $c_1$  expresses a constant for the image area outside of both models,  $c_2$  for the image area between outer and inner models, and  $c_3$  for the image region lies to the interior of both models. With the assumption that  $I$  consists of two regions  $I1$  and  $I2$  with boundary  $C_o$ ,  $C_{out}$  and  $C_{in}$  the boundaries of the outer and inner deformable models used (Section 2), it is obvious that  $C_o$  is the minimizer of the ‘‘fitting’’ term:

$$\begin{aligned} & \inf_C \{F_1(C_{out}, C_{in}) + F_2(C_{out}, C_{in}) + F_3(C_{out}, C_{in})\} \\ & \approx 0 \\ & \approx F_1(C_o, C_o) + F_2(C_o, C_o) + F_3(C_o, C_o). \end{aligned}$$

This can be seen easily. For instance, if models  $C_{out}$  and  $C_{in}$  are both outside the object, then  $F_1(C_{out}, C_{in}) \approx 0$ ,  $F_2(C_{out}, C_{in}) \approx 0$  and  $F_3(C_{out}, C_{in}) > 0$ . If the models  $C_{out}$  and  $C_{in}$  are both inside the object, then  $F_1(C_{out}, C_{in}) > 0$ ,  $F_2(C_{out}, C_{in}) \approx 0$  and

$F3(C_{out}, C_{in}) \approx 0$ . If the model  $C_{out}$  is outside the object while  $C_{in}$  is inside, then  $F1(C_{out}, C_{in}) \approx 0$ ,  $F2(C_{out}, C_{in}) > 0$  and  $F3(C_{out}, C_{in}) \approx 0$ . If the models  $C_{out}$  and  $C_{in}$  are both inside and outside the object, then  $F1(C_{out}, C_{in}) > 0$ ,  $F2(C_{out}, C_{in}) > 0$  and  $F3(C_{out}, C_{in}) > 0$ . Finally, the fitting energy is minimized if  $C_{out} = C_{in} = C_o$ , i.e., if the models  $C_{out}$  and  $C_{in}$  are on the boundary of the object. That is, the fitting term is minimized when the outer and inner models of the dual deformable model converged to each other and to the object boundary  $C_o$ . These basic marks are illustrated in Figure 2.

In our model, we will minimize the above fitting term and we will add some regularizing terms, like the length of the models  $C_{out}$  and  $C_{in}$ , and the area of the region between models  $C_{out}$  and  $C_{in}$ . Therefore, we introduce the energy functional  $F(C_{out}, C_{in})$ , given by:

$$\begin{aligned} F(C_{out}, C_{in}) = & \mu_1 \cdot Length(C_{out}) + \mu_2 \cdot Length(C_{in}) + \nu \cdot Area(between(C_{out}, C_{in})) \\ & + \lambda_1 \int_{\substack{outside(C_{out}) \\ outside(C_{in})}} |I(x, y) - c_1|^2 dx dy + \lambda_2 \int_{\substack{inside(C_{out}) \\ outside(C_{in})}} |I(x, y) - c_2|^2 dx dy \\ & + \lambda_3 \int_{\substack{inside(C_{out}) \\ inside(C_{in})}} |I(x, y) - c_3|^2 dx dy \end{aligned} \quad (15)$$

where  $\mu_1, \mu_2 \geq 0, \nu \geq 0, \lambda_1, \lambda_2, \lambda_3 > 0$  are fixed parameters. If  $C_o$  solves:

$$F(C_o, C_o) = \inf_C F(C), \quad (16)$$

that  $C_o$  is the solution to the segmentation problem (object boundary). The first two terms, in the definition of  $F(15)$ , accounts for smoothing  $C_{out}$  and  $C_{in}$  and the third term forces model  $C_{out}$  to move inward and  $C_{in}$  to move outward, if  $\nu$  is large.

**3.2. Level-Set Formulation.** In the level set method [5],  $C_{out} \subset I$  and  $C_{in} \subset I$  are represented by the zero level set of Lipschitz function  $\phi_{out} : I \rightarrow \mathbb{R}$ , such that:

$$\begin{cases} C_{out} & = \{(x, y) \in I : \phi_{out}(x, y) = 0\}, \\ inside(C_{out}) & = \{(x, y) \in I : \phi_{out}(x, y) > 0\}, \\ outside(C_{out}) & = \{(x, y) \in I : \phi_{out}(x, y) < 0\}, \end{cases} \quad (17)$$

and  $\phi_{in} : I \rightarrow \mathbb{R}$ :

$$\begin{cases} C_{in} & = \{(x, y) \in I : \phi_{in}(x, y) = 0\}, \\ inside(C_{in}) & = \{(x, y) \in I : \phi_{in}(x, y) > 0\}, \\ outside(C_{in}) & = \{(x, y) \in I : \phi_{in}(x, y) < 0\}, \end{cases} \quad (18)$$

Figure 3 illustrates the above assumptions and notations on the level set functions  $\phi_{out}$  and  $\phi_{in}$ , defining the evolving models  $C_{out}$  and  $C_{in}$ . For more details, we refer the reader to [5].

For the level set formulation of our variational dual deformable model, we represent models  $C_{out}$  and  $C_{in}$  by the unknown variables  $\phi_{out}$  and  $\phi_{in}$ .

Recall the definition of the Heaviside function  $H(s)$  to be:

$$H(s) = \begin{cases} 1, & \text{if } s \geq 0 \\ 0, & \text{if } s < 0, \end{cases} \quad (19)$$

and  $\delta(s)$ , the Dirac delta function, to be the distributional derivative of  $H(s)$ . Noting that:

$$\begin{aligned} length\{C_{out}\} &= \int_I \nabla H(\phi_{out}(x, y)) dx dy \\ length\{C_{in}\} &= \int_I \nabla H(\phi_{in}(x, y)) dx dy \end{aligned}$$

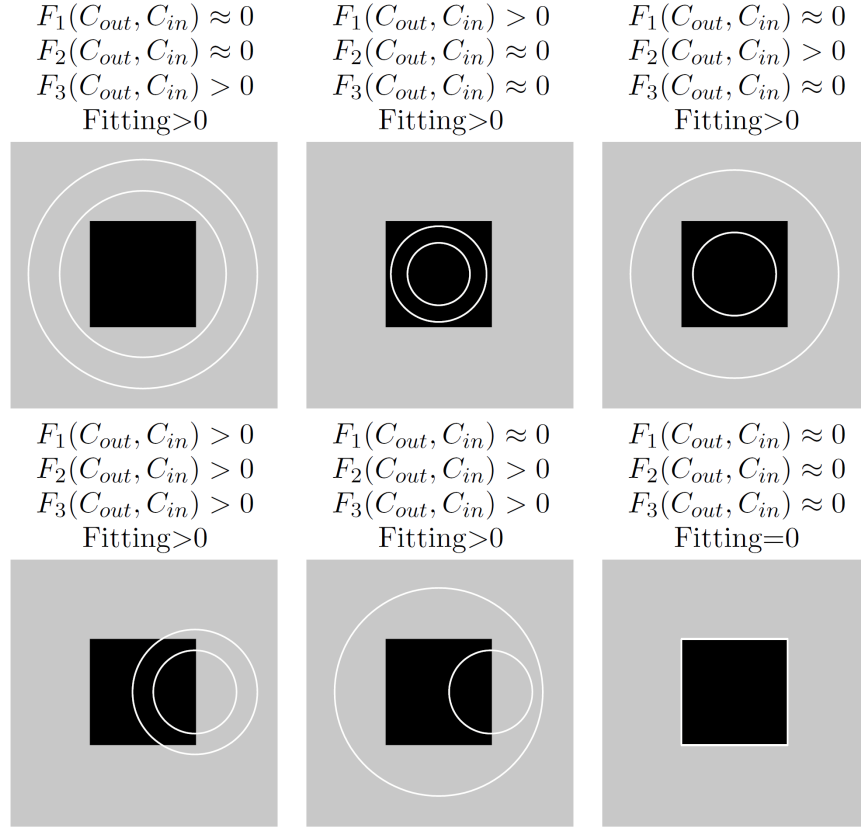


FIGURE 2. Consider all possible cases in the position of the models  $C_{out}$  and  $C_{in}$ . The fitting term is minimized only when the models are on the boundary of the object.

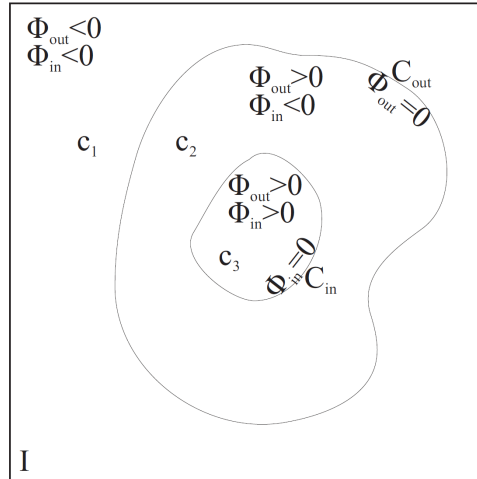


FIGURE 3. Models  $C_{out}$  and  $C_{in}$  and properties of the image  $I$  regarding them.

$$\text{Area}\{\text{between}(C_{out}, C_{in})\} = \int_I H(\phi_{out}(x, y)) [1 - H(\phi_{in})] dx dy,$$

and

$$\int_{\substack{\text{outside}(C_{out}) \\ \text{outside}(C_{in})}} |I(x, y) - c_1|^2 dx dy = \int_I |I(x, y) - c_1|^2 [1 - H(\phi_{out})] [1 - H(\phi_{in})] dx dy,$$

$$\int_{\substack{\text{outside}(C_{out}) \\ \text{outside}(C_{in})}} |I(x, y) - c_2|^2 dx dy = \int_I |I(x, y) - c_2|^2 H(\phi_{out}) [1 - H(\phi_{in})] dx dy,$$

$$\int_{\substack{\text{outside}(C_{out}) \\ \text{outside}(C_{in})}} |I(x, y) - c_3|^2 dx dy = \int_I |I(x, y) - c_3|^2 H(\phi_{out}) H(\phi_{in}) dx dy,$$

we can rewrite the energy  $F(C_{out}, C_{in})$  (15) in the following way:

$$\begin{aligned} F(\phi_{out}, \phi_{in}) &= \mu_1 \int_I \delta(\phi_{out}(x, y)) |\nabla \phi_{out}(x, y)| dx dy + \mu_2 \int_I \delta(\phi_{in}(x, y)) |\nabla \phi_{in}(x, y)| dx dy \\ &+ \nu \int_I H(\phi_{out}(x, y)) [1 - H(\phi_{in})] dx dy + \lambda_1 \int_I |I(x, y) - c_1|^2 [1 - H(\phi_{out})] [1 - H(\phi_{in})] dx dy \\ &+ \lambda_2 \int_I |I(x, y) - c_2|^2 H(\phi_{out}) [1 - H(\phi_{in})] dx dy + \lambda_3 \int_I |I(x, y) - c_3|^2 H(\phi_{out}) H(\phi_{in}) dx dy \end{aligned} \quad (20)$$

where constants  $c_1$ ,  $c_2$  and  $c_3$  expressed by functions  $\phi_{out}$  and  $\phi_{in}$  by:

$$c_1 = \frac{\int_I I(x, y) [1 - H(\phi_{out})] [1 - H(\phi_{in})] dx dy}{\int_I [1 - H(\phi_{out})] [1 - H(\phi_{in})] dx dy}, \quad (21)$$

if  $\int_I [1 - H(\phi_{out})] [1 - H(\phi_{in})] dx dy > 0$  (i.e. if the model  $C_{out}$  has a nonempty exterior in  $I$ ), and

$$c_2 = \frac{\int_I I(x, y) H(\phi_{out}) [1 - H(\phi_{in})] dx dy}{\int_I H(\phi_{out}) [1 - H(\phi_{in})] dx dy}, \quad (22)$$

if  $\int_I H(\phi_{out}) [1 - H(\phi_{in})] dx dy > 0$  (i.e. if the area between models  $C_{out}$  and  $C_{in}$  is nonempty in  $I$ ), and

$$c_3 = \frac{\int_I I(x, y) H(\phi_{out}) H(\phi_{in}) dx dy}{\int_I H(\phi_{out}) H(\phi_{in}) dx dy}, \quad (23)$$

if  $\int_I H(\phi_{out}) H(\phi_{in}) dx dy > 0$  (i.e. if the model  $C_{in}$  has a nonempty interior in  $I$ ).

**3.3. Functional Minimization.** As stated in the energy definition, we seek to minimize  $F(C_{out}, C_{in})$  (20) with respect to  $C_{out}$  and  $C_{in}$ , i.e., to  $\phi_{out}$  and  $\phi_{in}$  which represent our models. From variational calculus, the minimization of a functional asks for the Euler-Lagrange equation to be solved. In order to compute the associated Euler-Lagrange equation for the unknown functions  $\phi_{out}$  and  $\phi_{in}$ , we consider slightly regularized versions of the functions  $H$  and  $\delta$ , denoted here by  $H_\varepsilon$  and  $\phi_\varepsilon$ , so that  $\delta_\varepsilon(x) = \nabla H_\varepsilon(x)$  in the strict sense of the derivative. Let us denote by  $F_\varepsilon(\phi_{out}, \phi_{in})$  the associated regularization functional, defined by:

$$\begin{aligned} F_\varepsilon(C_{out}, C_{in}) &= \\ &\mu_1 \int_I \delta_\varepsilon(\phi_{out}(x, y)) |\nabla \phi_{out}(x, y)| dx dy + \mu_2 \int_I \delta_\varepsilon(\phi_{in}(x, y)) |\nabla \phi_{in}(x, y)| dx dy \\ &+ \nu \cdot \int_I H_\varepsilon(\phi_{out}(x, y)) [1 - H_\varepsilon(\phi_{in})] dx dy + \lambda_1 \int_I |I(x, y) - c_1|^2 [1 - H_\varepsilon(\phi_{out})] dx dy \\ &+ \lambda_2 \int_I |I(x, y) - c_2|^2 H_\varepsilon(\phi_{out}) [1 - H_\varepsilon(\phi_{in})] dx dy + \lambda_3 \int_I |I(x, y) - c_3|^2 H_\varepsilon(\phi_{out}) H_\varepsilon(\phi_{in}) dx dy, \end{aligned} \quad (24)$$

Keeping  $c_1, c_2$  and  $c_3$  fixed, and minimizing  $F_\varepsilon$  with respect to  $\phi_{out}$  and  $\phi_{in}$ , we deduce the associated Euler-Lagrange equation both for  $\phi_{out}$  and  $\phi_{in}$ . Parameterizing the descent direction by an artificial time  $t \geq 0$ , the equation in  $\phi_{out}(t, x, y)$  as well as in  $\phi_{in}(t, x, y)$  (with  $\phi_{out}(0, x, y)$  and  $\phi_{in}(0, x, y)$  defining the initial position of the model) is:

$$\begin{aligned} \frac{\partial \phi_{out}}{\partial t} &= \delta_\varepsilon(\phi_{out}) \left[ \mu_1 \operatorname{div} \left( \frac{\nabla \phi_{out}}{|\nabla \phi_{out}|} \right) - \nu + \lambda_1 (I - c_1)^2 - \lambda_2 (I - c_2)^2 \right] \\ &= 0 \\ \frac{\delta_\varepsilon \phi_{out}}{|\nabla \phi_{out}|} \frac{\partial \phi_{out}}{\partial \vec{n}} &= 0 \text{ on } \partial I, \end{aligned} \quad (25)$$

$$\begin{aligned} \frac{\partial \phi_{in}}{\partial t} &= \delta_\varepsilon(\phi_{in}) \left[ \mu_2 \operatorname{div} \left( \frac{\nabla \phi_{in}}{|\nabla \phi_{in}|} \right) - \nu + \lambda_2 (I - c_2)^2 - \lambda_3 (I - c_3)^2 \right] \\ &= 0 \\ \frac{\delta_\varepsilon \phi_{in}}{|\nabla \phi_{in}|} \frac{\partial \phi_{in}}{\partial \vec{n}} &= 0 \text{ on } \partial I, \end{aligned} \quad (26)$$

where  $\vec{n}$  denotes the exterior normal to the boundary  $\partial I$ , and  $\partial \phi_{out}/\partial \vec{n}$  and  $\partial \phi_{in}/\partial \vec{n}$  denote the normal derivatives of  $\phi_{out}$  and  $\phi_{in}$  at the boundary. In order model to reach to a steady state, equations (25) and (26) must be satisfied, and hence the functional (20) is minimized. The zero level-set of  $\phi_{out}$  and  $\phi_{in}$  at the steady state is the curve  $C_o$ , which solves the segmentation problem.

**3.4. Numerical Approximation of the Energy.** Firstly, the regularization of  $H$  and  $\delta$  functions, namely  $H_\varepsilon$  and  $\delta_\varepsilon$ , respectively, used in our computations is the following:

$$\begin{aligned} H_\varepsilon(s) &= \frac{1}{2} \left( 1 + \frac{2}{\pi} \arctan \left( \frac{s}{\varepsilon} \right) \right), \\ \delta_\varepsilon(s) &= \frac{1}{\pi} \frac{\varepsilon}{\varepsilon^2 + s^2}. \end{aligned} \quad (27)$$

This distinct approximation and regularization of the functions  $H_\varepsilon$  and  $\delta_\varepsilon$  (taking  $\delta_\varepsilon = H'_\varepsilon$ ) are presented in Figure 4. As  $\varepsilon \rightarrow 0$ , the regularized functions converge to  $H$  and  $\delta$ . Also, these functions are different to zero everywhere, tending not to zero our energy in any case except in its minimization state.

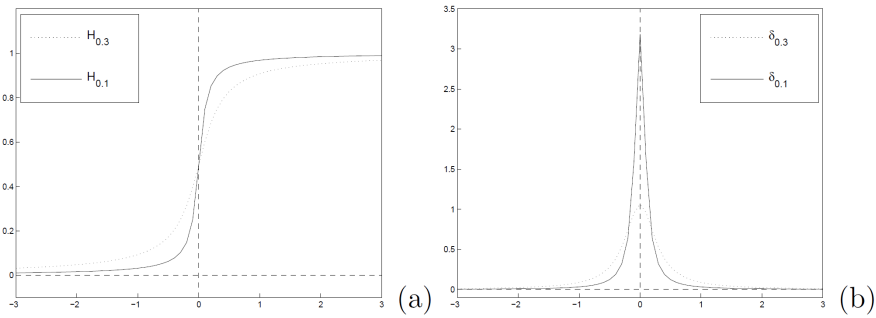


FIGURE 4. (a) Regularized Heaviside function  $H_\varepsilon$  for  $\varepsilon = 0.1$  and  $\varepsilon = 0.3$ , and (b) regularized Delta function  $\delta_\varepsilon$  for  $\varepsilon = 0.1$  and  $\varepsilon = 0.3$ .

To discretize the energy equation in  $\phi_{out}$  and in  $\phi_{in}$ , we use a finite differences implicit scheme. Let us first define some notations: let  $h$  be the space step,  $\Delta t$  be the time step, and  $(x_i, y_i) = (i_h, j_h)$  be the grid points,  $1 \leq i, j \leq M$ . Let  $\phi_{out}^n(i, j) = \phi_{out}(n\Delta t, x_i, y_i)$  be an approximation of  $\phi_{out}(t, x, y)$ , and  $\phi_{in}^n(i, j) = \phi_{in}(n\Delta t, x_i, y_i)$  an approximation of  $\phi_{in}(t, x, y)$ , with  $n \geq 0$ ,  $\phi_{out}^0(i, j) = \phi_{out}(0, x_i, y_i)$ ,  $\phi_{in}^0(i, j) = \phi_{in}(0, x_i, y_i)$ . The finite differences are:

$$\begin{aligned}
\Delta_-^x \phi(i, j) &= \phi(i, j) - \phi(i-1, j), \\
\Delta_+^x \phi(i, j) &= \phi(i+1, j) - \phi(i, j), \\
\Delta_-^y \phi(i, j) &= \phi(i, j) - \phi(i, j-1), \\
\Delta_+^y \phi(i, j) &= \phi(i, j+1) - \phi(i, j),
\end{aligned} \tag{28}$$

where  $\phi(i, j)$  is thought either  $\phi_{out}(i, j)$  or  $\phi_{in}(i, j)$ .

Knowing  $\phi_{out}^n$  and  $\phi_{in}^n$ ,  $c_1$ ,  $c_2$  and  $c_3$  using (21), (22) and (23), respectively, can be computed. Then, we can compute  $\phi_{out}^{n+1}$  out by the following discretization and linearization (forward implicit scheme presented in [22]) of (25) in  $\phi_{out}$ :

$$\begin{aligned}
\frac{\phi_{out}^{n+1}(i, j) - \phi_{out}^n(i, j)}{\Delta t} &= \\
\delta_h(\phi_{out}^n(i, j)) &\left[ \frac{\mu_1}{h^2} \Delta_-^x \left( \frac{\Delta_+^x \phi_{out}^{n+1}(i, j)}{\sqrt{\frac{(\Delta_+^x \phi_{out}^n(i, j))^2}{h^2} + \frac{(\phi_{out}^n(i, j+1) - \phi_{out}^n(i, j-1))^2}{4h^2}}} \right) \right. \\
&+ \frac{\mu_1}{h^2} \Delta_-^y \left( \frac{\Delta_+^y \phi_{out}^{n+1}(i, j)}{\sqrt{\frac{(\Delta_+^y \phi_{out}^n(i, j))^2}{h^2} + \frac{(\phi_{out}^n(i+1, j) - \phi_{out}^n(i-1, j))^2}{4h^2}}} \right) \\
&\left. - \nu + \lambda_1 (I(i, j) - c_1)^2 - \lambda_2 (I(i, j) - c_2)^2 \right], \tag{29}
\end{aligned}$$

and  $\phi_{in}^{n+1}$  in of (26) in  $\phi_{in}$  is:

$$\begin{aligned}
\frac{\phi_{in}^{n+1}(i, j) - \phi_{in}^n(i, j)}{\Delta t} &= \\
\delta_h(\phi_{in}^n(i, j)) &\left[ \frac{\mu_1}{h^2} \Delta_-^x \left( \frac{\Delta_+^x \phi_{in}^{n+1}(i, j)}{\sqrt{\frac{(\Delta_+^x \phi_{in}^n(i, j))^2}{h^2} + \frac{(\phi_{in}^n(i, j+1) - \phi_{in}^n(i, j-1))^2}{4h^2}}} \right) \right. \\
&+ \frac{\mu_1}{h^2} \Delta_-^y \left( \frac{\Delta_+^y \phi_{in}^{n+1}(i, j)}{\sqrt{\frac{(\Delta_+^y \phi_{in}^n(i, j))^2}{h^2} + \frac{(\phi_{in}^n(i+1, j) - \phi_{in}^n(i-1, j))^2}{4h^2}}} \right) \\
&\left. - \nu + \lambda_2 (I(i, j) - c_2)^2 - \lambda_3 (I(i, j) - c_3)^2 \right], \tag{30}
\end{aligned}$$

This linear system is solved via the Jacobi iterative method, and for more details, we refer the reader to [38].

**3.5. Reinitialization.** At each time step, when  $\phi_{out}^{n+1}$  and  $\phi_{in}^{n+1}$  are computed from  $\phi_{out}$  and  $\phi_{in}$ , respectively, the  $\delta_h(\cdot)$  term, in the scheme, causes sharp gradients in both  $\phi_{out}$  and  $\phi_{in}$  (i.e.  $|\nabla \phi_{out}| \neq 1$  and  $|\nabla \phi_{in}| \neq 1$  after a finite amount of time. Maintaining  $\phi_{out}$  and  $\phi_{in}$  as distance “like” functions is essential for providing the interface with a width fixed in time. Computation of  $\delta_h(\cdot)$  is difficult to be computed near a steep gradient (“shocks”) in the distance function. The values of  $\delta_h(\cdot)$ , especially for large density ratios, will be greatly distorted if  $|\nabla \phi_{out}|$  and/or  $|\nabla \phi_{in}|$  are far from one. Thus, the presence of such shocks may cause difficulty in the computation [39].

This is resolved by reinitializing  $\phi_{out}^{n+1}$  and  $\phi_{in}^{n+1}$  to the signed distance function to its zero-level curve. This prevents the level set function to become too flat, or it can be seen as a rescaling and regularization. For our algorithm, the reinitialization is optional. It can be implemented by solving the following evolution equation [39] (we use the term  $p$  in the following equations, but the same procedure stands for each  $\phi_{out}$  and  $\phi_{in}$ ):

$$\begin{aligned}\psi_t &= \text{sign}(\phi^n)(1 - |\nabla\psi|) \\ \phi(0, \cdot) &= \phi^n(\cdot),\end{aligned}\quad (31)$$

where  $\phi(t, \cdot)$  is our solution  $\phi$  at time  $t$ . Then the new  $\phi(t, \cdot)$  will be r, such as obtained at the steady state of (31). The solution  $\psi(t, \cdot)$  of (31) will have the same zero-level set as  $\phi(t, \cdot)$  and away from this set,  $|\nabla\psi|$  will converge to 1. To discretize the equation (31), we use the scheme proposed in [39]. The numerical scheme in solving this is as follows. Let:

$$\psi^{k+1}(i, j) = \psi^k(i, j) - \Delta t(\text{sign}(\phi^n))G(\psi^k(i, j)), \quad (32)$$

where  $G(\psi(i, j))$  is defined as:

$$\begin{cases} \frac{\sqrt{\max_{a^+, b^-} + \max_{c^+, d^-}}}{h} - 1, & \text{if } \phi^n(i, j) > 0 \\ \frac{\sqrt{\max_{a^-, b^+} + \max_{c^-, d^+}}}{h} - 1, & \text{if } \phi^n(i, j) < 0 \\ 0, & \text{otherwise,} \end{cases} \quad (33)$$

where  $\max_{a^+, b^-} = \max((a^+)^2, (b^-)^2)$ ,  $\max_{c^+, d^-} = \max((c^+)^2, (d^-)^2)$  and so on, and  $a^+ = \max(\Delta_x^- \psi(i, j), 0)$ ,  $c^+ = \max(\Delta_y^- \psi(i, j)/h, 0)$ ,  $d^+ = \max(\Delta_y^+ \psi(i, j)/h, 0)$ ,  $a^- = \min(\Delta_x^- \psi(i, j)/h, 0)$ ,  $b^+ = \min(\Delta_x^+ \psi(i, j)/h, 0)$ , and so on.

In general, the bulk of the computation time is spend during the reinitialization procedure.

**3.6. Final Dual Deformable Model.** The energy function we already presented, is used as the motivation power function of the dual deformable model presented in Section 2. The exterior model (outer) uses the implicit function (29), while the interior model (inner) uses function (30). The intermediate model does not uses any power energy function, but the deformations of the other two model, which are interconnected to each other, deform it as well. Thus, at each iteration step of the above described procedure, we calculate  $\phi_{out}^{n+1}$  and  $\phi_{in}^{n+1}$ , and the difference between the dual deformable model position ( $C_{out}^n$  and  $C_{in}^n$ ) with the curves  $\phi_{out}^{n+1}(x, y) = 0$  and  $\phi_{in}^{n+1}(x, y) = 0$  is used as the motivation force of the introduced dual model. These differences could be calculated using signed distance maps of the curves  $\phi_{out}^{n+1}$  and  $\phi_{in}^{n+1}$  [40, 41, 42]. The deformation of the model give us the new position of the model ( $\phi_{out}^{n+1}$  and  $\phi_{in}^{n+1}$ ). However, after dual model deformation, the  $\phi_{out}^{n+1}$  and  $\phi_{in}^{n+1}$  in are reinstalled based on  $C_{out}^{n+1}$  and  $C_{in}^{n+1}$  in order to be synchronized with the dual model position. This procedure is repeated until model motivation energy is minimized, i.e., until the energy becomes stationary forcing the model to stop moving.

Due to the fact that all three models are coupled using springs (which cause them to be attracted to each other) and the nature of energy (which causes model to be attracted to suitable image features), stationary model state usually occurs when all three models have converged to each other and all together to the boundary of the object under determination. That is, thorough the iterative process, the outer model converges to the inner, the inner to the outer, and both converge to the object boundary. The intermediate model of the dual deformable model, finally, provides us the object boundary.

The overall dual deformation model algorithm is summarized as follows:

- step1** : Initialize the physics - based dual deformable model ( $C_{out}^1$  and  $C_{in}^1$ ).
- step2** : Initialize  $\phi_{out}^0$  and  $\phi_{in}^0$  based on the dual model position.
- step3** : Compute  $c_1$ ,  $c_2$  and  $c_3$  by (21), (22) and (23) respectively.
- step4** : Solve (25) and (26) to obtain  $\phi_{out}^{n+1}$  and  $\phi_{in}^{n+1}$ .
- step5** : Calculate the motivation force using signed distance maps of curves  $\phi_{out}^{n+1}$  and  $\phi_{in}^{n+1}$ .
- step6** : Deform the dual model.

- step7** : Adapt  $\phi_{out}^{n+1}$  and  $\phi_{in}^{n+1}$  to be synchronized with model position ( $C_{out}^{n+1}$  and  $C_{in}^{n+1}$ ).
- step8** : Reinitialize  $\phi_{out}$  and  $\phi_{in}$  locally to the signed distance function to the curve (this step is optional).
- step9** : Check whether the solution is stationary. If not,  $n = n + 1$  and returns to step 3.

Figure 5 depicts the detection of different objects exploiting the introduced method. It is shown, in the intermediate steps, the convergence of the outer model to the inner and the opposite (inner model converges to the outer), and how all three interconnected models of the dual deformation scheme converges to the boundary of the objects. The stationary (final) state of the dual model lies on the boundary of all the detected objects in the image, which occurs when outer and inner model (and as a consequence the intermediate model) converge to each other and to the objects boundary.

The left image of each pair of images in Figure 5 depicts the dual deformable model during the object boundary detection, while the right shows only the intermediate model.

**4. Experimental Results.** In this Section, we show the performance of our method by presenting numerical results using our dual deformable model on various synthetic and real images, with different types of contours and shapes. We show the active contour evolving in the original image  $I$ , and the associated piecewise-constant approximation of  $I$  (given by the averages  $c_1$ ,  $c_2$  and  $c_3$ ). In our numerical experiments, we generally choose the parameters as follows:  $\lambda_1 = \lambda_3 = 1, \lambda_2 = 2, \mu_1 = \mu_2 = 1, \nu = 1, h = 1$  (the step space),  $\Delta t = 0.1$  (the time step). Only the characteristic value  $a$  (Section 2) of the dual deformable model, which has a scaling like role, is not the same in all experiments. If we have to detect all or as many objects as possible and of any size, then  $a$  will be small. If we have to detect only larger objects and to not detect smaller objects (like points/pixels, due to noise), then  $a$  has to be larger.

The selection of the parameter  $a$  has been performed by trial-and-error method selecting the one with the best performance. Furthermore, the model is randomly initiated on the image. Also, all the experiments have been performed without the re-initialization step. The adaptation step between  $\phi_{out}$  and  $\phi_{in}$  curves and the dual deformable model in order to be synchronized, corrects the problem handled by the re-initialization step.

The length parameters  $\mu_1$  and  $\mu_2$ , have a scaling role as well. This means that if  $\mu_1, \mu_2 \gg 1$ , then a few large closed curves will retain in the steady state, compared to many small ones. This may be useful in grouping objects of similar characteristics (“chromatic resemblance”). The area parameter  $\nu$  controls the importance of area between the outer and inner model. If  $\nu \gg 1$ , it forces the outer model to move strictly inward, while the inner model strictly outward. Also, the speed at which models converge increases. Finally, the relative balance between  $\lambda_1$ ,  $\lambda_2$  and  $\lambda_3$  determines which side, inside, outside or intermediate, has higher importance in minimizing  $\int_I |I - c_i| dx dy$ . This is useful in segmenting blurred images, e.g.,  $\lambda_3 > \lambda_2 > \lambda_1$  ensure that the blurred object will be completely enclosed. All these properties will be verified in the experimental results.

In Figure 6, we show how our dual deformable model works on a synthetic image with various shapes. Figures 7 and 8 depict the way our model converges at the objects on noisy synthetic images containing various objects. In this experiments was used Gaussian (Figure 7) and uniform noise (Figure 8) as well. Due to the fact that models are interconnected with springs, it is shown that dual model has a remarkable resistance to noise, converging almost like at a “clea” (without noise) image. In this experiment, the characteristic value  $a$  was set equal to 20 ( $a = 20$ ), enforcing the model to “ignore” the

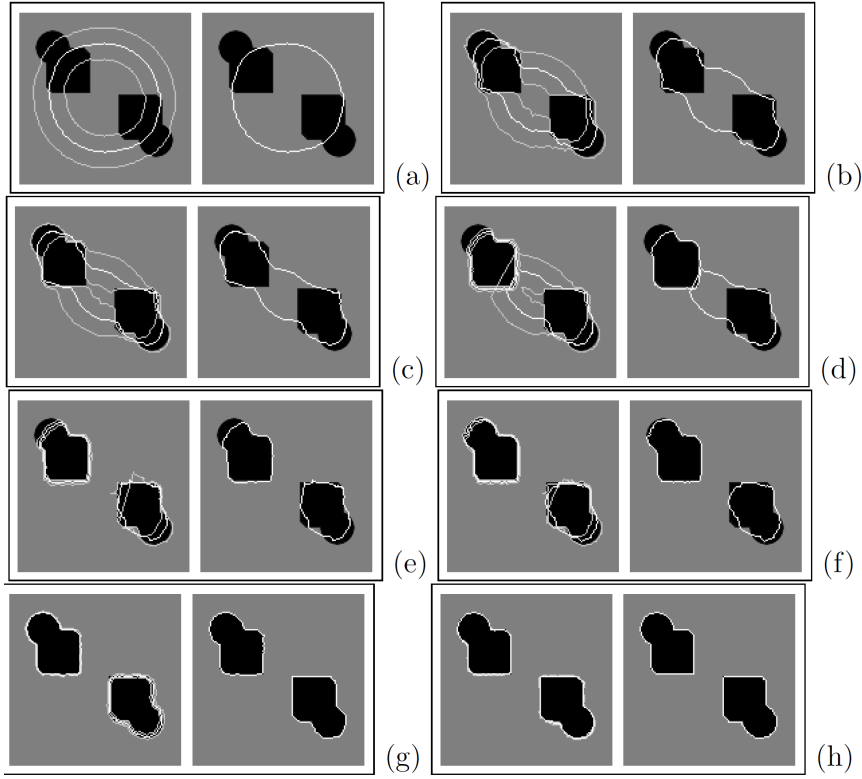


FIGURE 5. *Object detection example exploiting the introduced method. Left: all three models during the convergence to the boundary of the objects. Right: the intermediate model.*

noise. Table 1 confirms the results in terms of the well known Tanimoto/Jaccard error [43]  $A(\cdot, \cdot)$  defined here as:

$$A(m, o) = 1 - \frac{\int_{C_o \cap C_m} dx dy}{\int_{C_o \cup C_m} dx dy}, \quad (34)$$

where  $C_m$  and  $C_o$  are the extracted and the desired contours respectively. In Table 1, the desired contour was extracted manually and compared using (34) with the extracted contours by the proposed method and the Chan-Vese method [22]. The errors of the proposed method are significantly less than the errors produced by the Chan-Vese method. Only the blurred images produce similar error, but still the proposed approach is better than that of Chan-Vese.

Furthermore, Figure 9 illustrates that the introduced dual model can detect different objects with blurred boundaries. Also, depending on the model parameters, we can enclose all blurred objects, or (as in our case) take an average like contour (intermediate model), since we do not let outer and inner models to fully converge to each other.

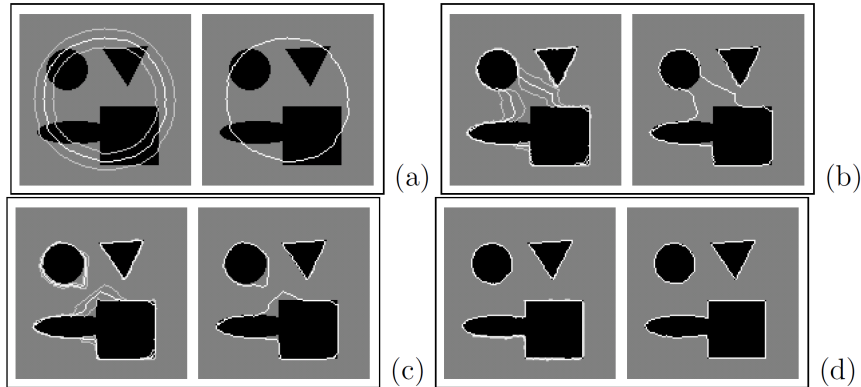


FIGURE 6. *Detection of different objects with various shapes. Left: all three models (dual deformable model) during convergence to the objects shape. Right: the intermediate model at the same steps. In this experiment model characteristic value was  $a = 1$ .*

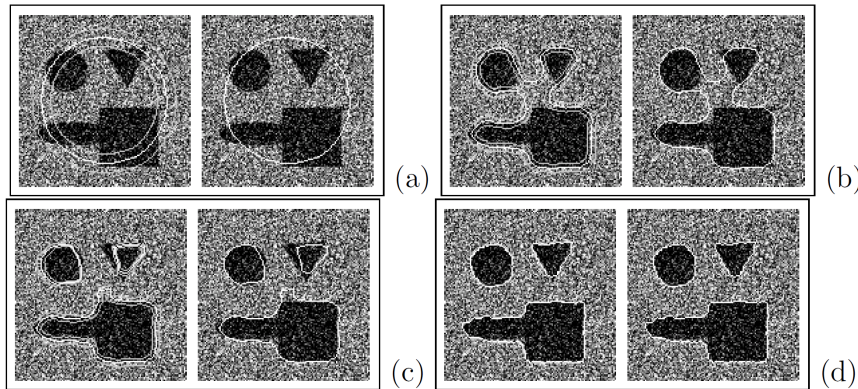


FIGURE 7. *Detection of different objects from a noisy image with various shapes (Gaussian noise). Left: all three models (dual deformable model) during convergence to the objects shape. Right: the intermediate model at the same steps. In this experiment model characteristic value  $a$  was  $a = 20$ .*

In the next example (Figure 10), we validate our model on a very different problem: to detect features in spatial point processes in the presence of substantial cluster. One application can be the detection of minefields using reconnaissance aircraft images that identify many objects that are not mines. These problems are usually solved using statistical methods (see [44] and [45]). By this application, we show again how our model can be used to detect objects or features with contours without gradient. This is not possible using classical snakes or active contours based on the gradient. The characteristic value of the model was set equal to  $a = 15$  in order to pass over the “noise” like points.

We also show examples on real images, with different types of contours or shapes, illustrating all the advantages of our model: the ability of detecting smooth boundaries, scale adaptivity, automatic change of topology, and robustness with respect to “noise”.

Some examples on real images (collected from the Internet) are illustrated in Figures 11, 12 and 14. The characteristic value of the model was set larger than the previous experiments ( $a \in [10, 15]$ ), in order to overpass the small objects spread all over the image and to detect those under consideration. It is shown, that the proposed algorithm

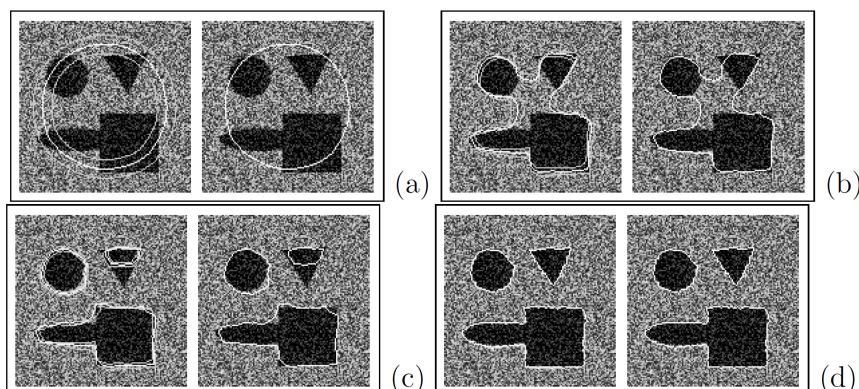


FIGURE 8. *Detection of different objects from a noisy image with various shapes (Uniform noise). Left: all three models (dual deformable model) during convergence to the objects shape. Right: the intermediate model at the same steps. In this experiment model characteristic value  $a$  was  $a = 20$ .*

TABLE 1. Area difference measure results.

Image	Proposed Method	Chan-Vese Method
Clear image	0.002	0.005
Noisy image (gaussian noise)	0.072	0.154
Noisy image (uniform noise)	0.053	0.121
Noisy image (speckle noise)	0.044	0.147
Blurred image	0.108	0.113
Real images (Figs. 11, 12, 14)	0.184	0.381

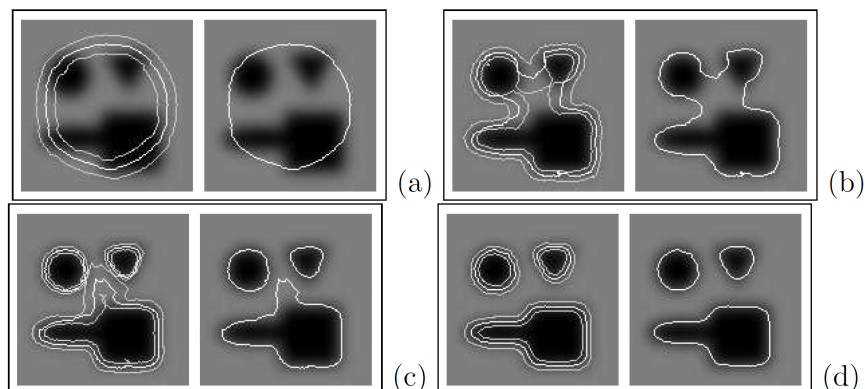


FIGURE 9. *Detection of three blurred objects. Left: all three models (dual deformable model) during convergence to the objects shape. Right: the intermediate model at the same steps. In this experiment model characteristic value  $a$  was  $a = 1$ .*

can work very effectively at real images as well, even in cases where the objects under consideration are more than one (Figure 14).

Furthermore, all the experiments described in this Section are applied to the Chan-Vese [22] method too. Figures 13 and 14 depict the results (the extracted contours) for both the proposed algorithm and the Chan-Vese method. The results of the introduced method are visually quite better, a fact that has been arithmetically confirmed in Table 1. The ground truth, in these examples, has been manually extracted and the Tanimoto/Jacard

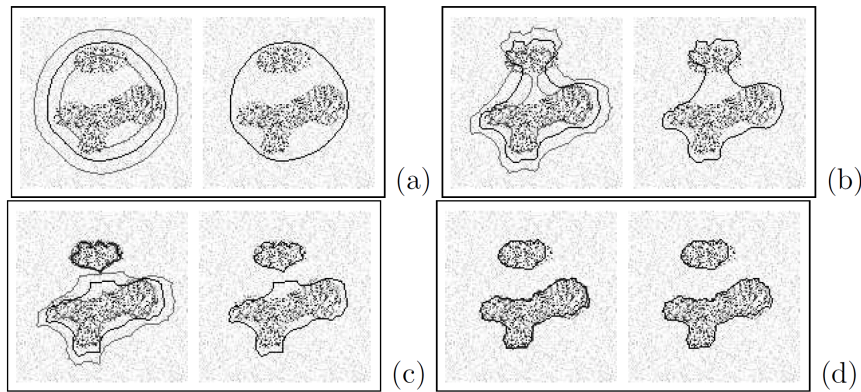


FIGURE 10. *Detection of a simulated minefield with contour without gradient. Left: all three models (dual deformable model) during convergence to the objects shape. Right: the intermediate model at the same steps. In this experiment model characteristic value  $a$  was  $a = 15$ .*

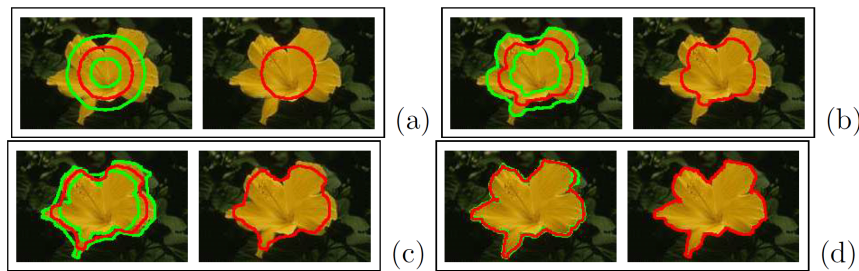


FIGURE 11. *Object detection on a real image. Left: all three models (dual de- formable model) during convergence to the objects shape. Right: the in- termediate model at the same steps. In this experiment model characteristic value  $a$  was  $a = 15$ .*

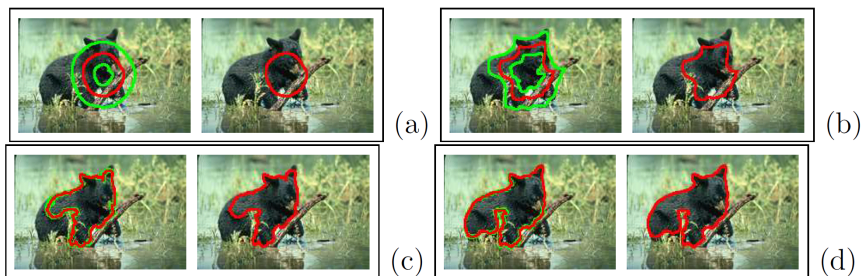


FIGURE 12. *Object detection on a real image. Left: all three models (dual de- formable model) during convergence to the objects shape. Right: the in- termediate model at the same steps. In this experiment model characteristic value  $a$  was  $a = 15$ .*

error measurement (34) placed in Table 1 (average error of all tested real images), confirms that the proposed algorithm provides better and more qualitative results, even in cases where the objects of interest are more than one.

Another interesting property of the proposed algorithm is that different values of the parameter  $a$  could produce different segmentation results. As the models characteristic

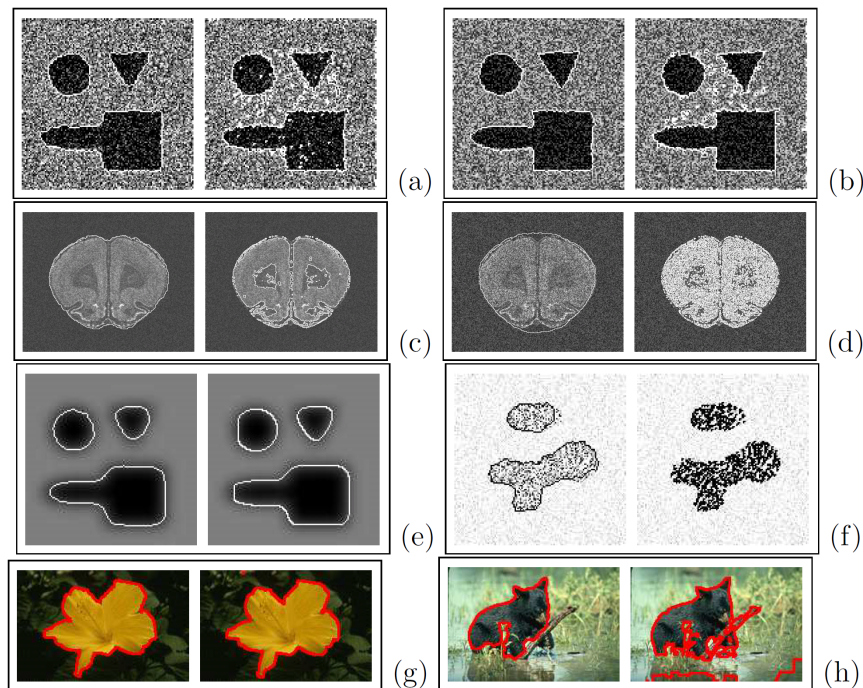


FIGURE 13. *Object detection by the proposed (left images) and the Chan-Vese method (right images). (a) image corrupted by gaussian noise, (b) by uniform noise, (c) by speckle noise, (d) by speckle noise (with different variance), (e) blurred image, (f) image with no sufficient gradient, (g) and (h) real images.*

value  $a$  is getting smaller then the deformable model is behaved as a fully deformable one producing oversegmentation results (Figure 15(a)). On the other hand, when the characteristic value  $a$  is getting larger, then the deformable model is more rigid and the segmentation result is grouping the objects under consideration (Figure 15(d)). Such an example is shown in Figure 15, where the proposed algorithm was applied on a noisy image with three objects using different values of the models characteristic value  $a$ .

Finally, Figure 16 illustrates the average computational cost for the proposed and the Chan-Vese algorithm compared above. Each image size has been tested to five different images. The proposed method is quite computational consuming, since it also involves the deformations of the model, but this drawback is compensated for its very good performance as it was shown above. All experiments were performed on a Pentium IV (3 GHz) workstation under Windows XP Professional without any particular code optimization.

However, the proposed method shares a problem with the Chan-Vese method, that is,

there are objects which cannot be detected using the intensity average only, i.e., texture images. Figure 17 illustrates four such examples that the averages “insid” and “outside” the curves are almost equal, and as a consequence the method will fail to detect the objects of interest. One way to overcome this difficulty, would be to use other information from the intensity of the initial image  $I$ , like the curvature, the orientation of level sets, or any other discriminant. That is, for image in Figure 17(a) we will replace in our method intensity  $I$  by *curvature* ( $I$ ) =  $div(\nabla I/|\nabla I|)$ . If the image under consideration is like the one in Figure 17(b), then intensity  $I$  will be replaced by *orientation* ( $I$ ) =  $\tan^{-1}(I_y/I_x)$  (the angle of the normal to the level curves). Furthermore, in Figures 17(c) and 17(d) the intensity  $I$  of the image could be replaced by any texture discriminant. In this framework, we refer the reader to [46].

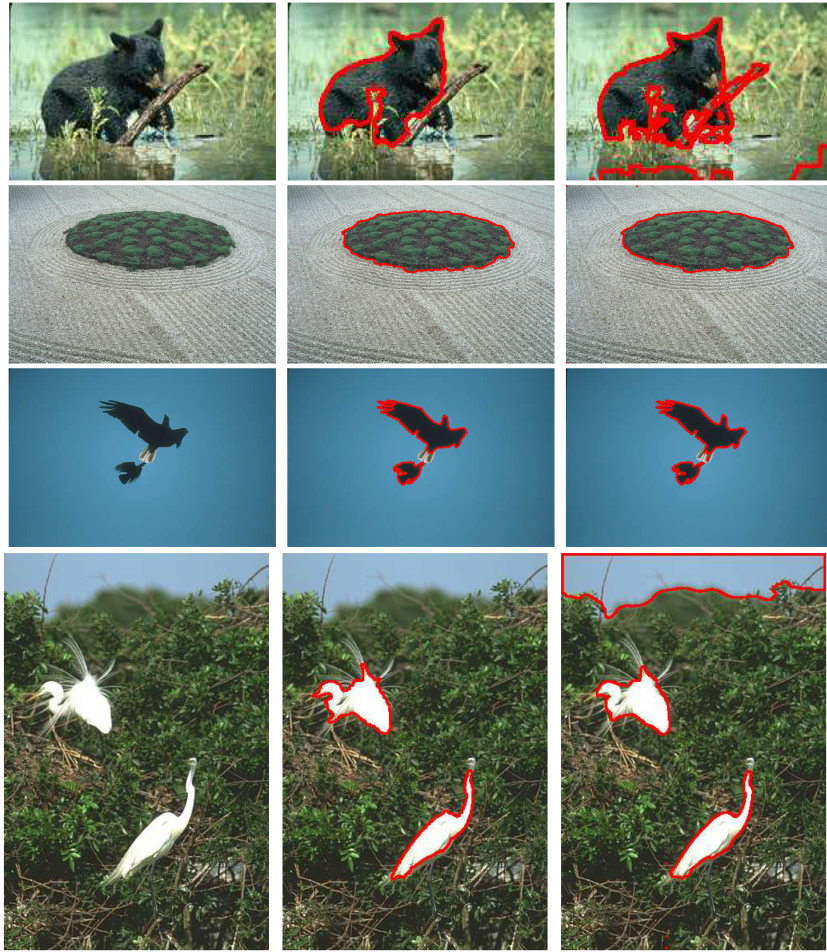


FIGURE 14. Object detection on real images (left column) by the proposed (middle column) and the Chan-Vese method (right column).

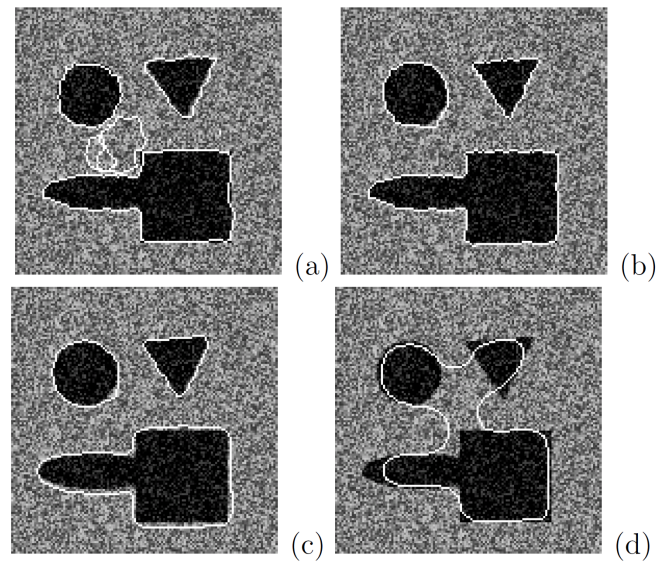


FIGURE 15. Object detection with different values of model parameter  $a$ . (a)  $a = 1$ , (b)  $a = 15$ , (c)  $a = 50$ , and (d)  $a = 500$ .

5. **Conclusion.** In this paper, we have introduced a novel physics-based dual deformable model for image segmentation. Our model can detect objects whose boundaries are not

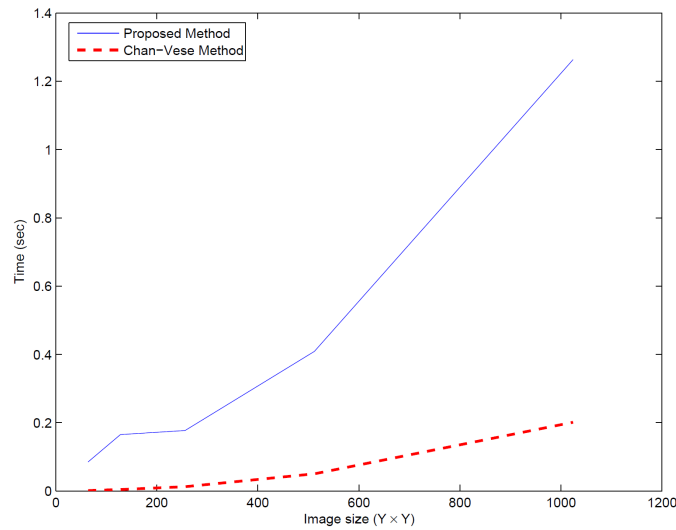


FIGURE 16. *Computational cost (in seconds) of the proposed and the Chan-Vese method.*

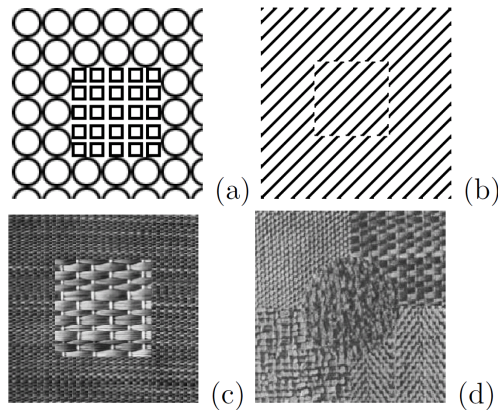


FIGURE 17. *Example of images that have almost equal intensity averages “inside” and “outside” the curves.*

necessarily defined by gradient, due to the fact that it is based on an energy minimization problem, and not on an edge-function as the most classical active contour models. This energy is used as the model motivation power evolving the deformable model, which will stop on the desired object boundary. Modal analysis was exploited in order to solve the deformation governing equations, and proportionally to model physical characteristics, a different segmentation result is produced every time. Three interconnected deformable models constitute the introduced dual deformable model. The main idea was captured by the fact that springs connect all three parts of the dual deformable model, enforce model to overpass local “minima” resulting to the desired global energy minimum. If a model “falls” in a local minima, the others “pull” it over and overcomes it, converging in that way to the global one. Thus, the whole model interconnection idea provides a balanced technique with a strong ability to reject “weak” local minima improving the performance of the segmentation against other known methods. Furthermore, the images under consideration do not need to be smoothed, even if they are noisy, and the location of their boundaries are very well detected and preserved. Objects, whose boundaries are not necessarily defined by gradient or with very smooth boundaries, can be detected very easily by the proposed dual deformable model.

Furthermore, the extension of the proposed dual deformable model to higher dimensions is an open research topic, since there are no explicit functions for the calculation of the deformations of the model in higher dimensions.

## REFERENCES

- [1] X. Munoz, J. Freixenet, X. Cufi and J. Marti, Strategies for image segmentation combining region and boundary information, *Pattern Recognition Letters*, vol. 24, no. 1, pp. 375-392, 2003.
- [2] M. Kass, A. Witkin and D. Terzopoulos, Snakes: active contour models, *International Journal of Computer Vision*, vol. 1, no. 4, pp. 321-331, 1988.
- [3] V. Caselles, F. Catte, T. Coll and F. Dibos, A geometric model for active contours in image processing, *Numerical Math*, vol. 66, no. 1, pp. 1-31, 1993.
- [4] R. Malladi, J. A. Sethian and B. C. Vemuri, Shape modeling with front propagation: A level set approach, *IEEE Trans. Pattern Analysis and Machine Intelligence*, vol. 17, no. 1, pp. 158-175, 1995.
- [5] S. Osher and J. A. Sethian, Fronts propagating with curvature-dependent speed: Algorithms based on hamilton-jacobi formulation, *Journal of Computational Physics*, vol. 79, pp. 12-49, 1988.
- [6] V. Caselles, R. Kimmel and G. Sapiro, Geodesic active contours, *International Journal of Computer Vision*, vol. 22, no. 1, pp. 61-79, 1997.
- [7] A. Yezzi, S. Kichenassamy, A. Kumar, P. Olver and A. Tannenbaum, A geometric snake model for segmentation of medical imagery, *IEEE Trans. Medical Imaging*, vol. 16, no. 2, pp. 199-209, 1997.
- [8] A. Sarti, C. Corsi, E. Mazzini and C. Lamberti, Maximum likelihood segmentation of ultrasound images with Rayleigh distribution, *IEEE Trans. Ultrasonics, Ferroelectrics, and Frequency Control*, vol. 25, no. 6, pp. 947-960, 2005.
- [9] H. Tek and B. Kimia, Image segmentation by reaction diffusion bubbles, *Proc. of International Conference on Computer Vision*, pp. 156-162, 1995.
- [10] L. Cohen and R. Kimmel, Global minimum for active contour models: A minimal path approach, *International Journal on Computer Vision*, vol. 24, no. 1, pp. 57-78, 1997.
- [11] L. Cohen, Multiple contour finding and perceptual grouping using minimal paths, *Journal of Mathematical Imaging and Vision*, vol. 14, no. 3, pp. 225-236, 2001.
- [12] S. Gunn and M. Nixon, A model based dual active contour, *Proc. of British Machine Vision Conference*, pp. 305-314, 1994.
- [13] S. R. Gunn and M. S. Nixon, A robust snake implementation: A dual active contour, *IEEE Trans. Pattern Analysis and Machine Intelligence*, vol. 19, no. 1, pp. 63-68, 1997.
- [14] G. Aboutanos, J. Nikanne, N. Watkins and B. Dawant, Model creation and deformation for the automatic segmentation of the brain in MR images, *IEEE Trans. Biomedical Engineering*, vol. 46, no. 11, pp. 1346-1356, 1999.
- [15] G. Giraldi, L. Goncalves and A. Oliveira, Dual topologically adaptable snakes, *Proc. of International Conference on Computer Vision, Pattern Recognition, and Image Processing*, pp. 103-107, 2000.
- [16] G. Georgoulas, G. Nikolakopoulos, Y. Koutroulis, A. Tzes and P. Groumpos, An intelligent visual-based system for object inspection and welding, relying on active contour models-algorithms, *Proc. of the 2nd Hellenic Conference on Artificial Intelligence*, pp. 399-410, 2002.
- [17] C. Erdem, A. Tekalp and B. Sankur, Video object tracking with feedback of performance measures, *IEEE Trans. Circuits and Systems for Video Technology*, vol. 13, no. 4, pp. 310-324, 2003.
- [18] M. Dawood, X. Jiang and K. Schafers, Reliable dual-band based contour detection: A double dynamic programming based approach, *Lecture Notes in Computer Science*, pp. 544-551, 2004.
- [19] N. Xu, R. Bansal and N. Ahuja, Object segmentation using graph cuts based active contours, *Proc. of IEEE International Conference on Computer Vision and Pattern Recognition*, vol. 2, pp. 46-53, 2003.
- [20] A. Chakraborty, L. Staib and J. Duncan, Deformable boundary finding in medical images by integrating gradient and region information, *IEEE Trans. Medical Imaging*, vol. 15, no. 6, pp. 859-870, 1996.
- [21] C. Samson, L. Blanc-Feraud, G. Aubert and J. Zerubia, A level set model for image classification, *International Journal of Computer Vision*, vol. 40, no. 3, pp. 187-197, 2000.
- [22] T. Chan and L. Vese, Active contours without edges, *IEEE Trans. Image Processing*, vol. 10, no. 2, pp. 266-277, 2001.
- [23] A. Tsai, A. Yezzi and A. Willsky, Curve evolution implementation of the Mumford-Shah functional for image segmentation, denoising, interpolation, and magnification, *IEEE Trans. Image Processing*, vol. 10, no. 8, pp. 1169-1186, 2001.

- [24] N. Paragios and R. Deriche, Geodesic active regions: A new framework to deal with frame partition problems in computer vision, *Journal of Visual Communication and Image Presentation*, vol. 13, no. 1, pp. 249-268, 2002.
- [25] A. Yezzi, A. Tsai and A. Willsky, A fully global approach to image segmentation via coupled curve evolution equations, *Journal of Visual Communication and Image Representation*, vol. 13, no. 1, pp. 195-216, 2002.
- [26] S. Jehan-Besson, M. Barlaud and G. Aubert, DREAM2s: Deformable regions driven by an eulerian accurate minimization method for image and video segmentation, *International Journal on Computer Vision*, vol. 53, no. 1, pp. 45-70, 2003.
- [27] S. Krinidis and V. Chatzis, Fuzzy energy-based active contours, *IEEE Trans. Image Processing*, vol. 18, no. 12, pp. 2747-2755, 2009.
- [28] S. Zhu and A. Yuille, Region competition: Unifying snakes, region growing, and Bayes/MDL for multiband image segmentation, *IEEE Trans. Pattern Analysis and Machine Intelligence*, vol. 18, no. 9, pp. 884-900, 1996.
- [29] S. Sclaroff and A. Pentland, Modal matching for correspondence and recognition, *IEEE Trans. Pattern Analysis and Machine Intelligence*, vol. 17, no. 6, pp. 545-561, 1995.
- [30] S. Krinidis and I. Pitas, Fast free vibration modal analysis of 2D physics-based deformable objects, *IEEE Trans. Image Processing*, vol. 14, no. 3, pp. 281-293, 2005.
- [31] C. Nastar and N. Ayache, Frequency-based nonrigid motion analysis: Application to four dimensional medical images, *IEEE Trans. Pattern Analysis and Machine Intelligence*, vol. 18, no. 11, pp. 1069-1079, 1996.
- [32] C. Nikou, G. Bueno, F. Heitz and J. P. Armspach, A joint physics-based statistical deformable model for multimodal brain image analysis, *IEEE Trans. Medical Imaging*, vol. 20, no. 10, pp. 1026-1037, 2001.
- [33] K. J. Bathe, *Finite Element Procedure*, New Jersey: Prentice Hall, Englewood Cliffs, 1996.
- [34] C. Nastar, *Modèles Physiques Déformables et Modes Vibratoires Pour L'analyse du Mouvement Non-rigide Dans les Images Multidimensionnelles*, Ph. D. Thesis, Ecole Nationale des Ponts et Chaussées, 1994.
- [35] G. Borgefors, On digital distance transforms in three dimensions, *Computer Vision and Image Understanding*, vol. 64, no. 3, pp. 368-376, 1996.
- [36] P. Danielsson, Euclidean distance transform, *Computer Graphics and Image Processing*, vol. 14, pp. 227-228, 1980.
- [37] A. Pentland and S. Sclaroff, Closed-form solutions for physically-based shape modeling and recognition, *IEEE Trans. Pattern Analysis and Machine Intelligence*, vol. 13, no. 7, pp. 715-729, 1991.
- [38] G. Aubert and L. Vese, A variational method in image recovery, *SIAM Journal on Numerical Analysis*, vol. 34, no. 5, pp. 1948-1979, 1997.
- [39] M. Sussman, P. Smerka and S. Osher, A level-set approach for computing solutions to incompressible two-phase flow, *Journal of Computational Physics*, vol. 114, no. 1, pp. 146-159, 1994.
- [40] G. Borgefors, Distance transformations in arbitrary dimensions, *Computer Vision, Graphics, and Image Processing*, vol. 27, pp. 321-345, 1984.
- [41] Gunilla Borgefors, Distance transformations in digital images, *Computer Vision, Graphics, and Image Processing*, vol. 34, no. 3, pp. 344-371, 1986.
- [42] G. Borgefors, Hierarchical chamfer matching: A parametric edge matching algorithm, *IEEE Trans. Pattern Analysis and Machine Intelligence*, vol. 10, pp. 849-965, 1988.
- [43] J. Tohka, Surface extraction from volumetric images using deformable meshes: A comparative study, *Proc. of the 7th European Conference on Computer Vision*, pp. 350-364, 2002.
- [44] S. Byers and A. Raftery, Nearest-neighbor clutter removal for estimating features in spatial point processes, *Journal of the American Statistical Association*, vol. 93, pp. 577-584, 1998.
- [45] A. Dasgupta and A. Raftery, Detecting features in spatial point processes with clutter via model-based clustering, *Journal of the American Statistical Association*, vol. 93, pp. 294-302, 1998.
- [46] C. Lopez and J. Morel, Axiomatization of shape analysis and application to texture hyper discrimination, *Proc. of IEEE Conference on Computer Vision and Pattern Recognition*, Berlin, Germany, pp. 646-647, 1993.